

Relaxation-Relaxation Correlation Spectroscopic Imaging (RR-CSI): Leveraging the Blessings of Dimensionality to Map In Vivo Microstructure

Daeun Kim¹, Jessica L. Wisnowski^{2,3}, Christopher T. Nguyen^{4,5,6}, Justin P. Haldar¹

¹Electrical Engineering, University of Southern California, Los Angeles, CA, USA

²Radiology, Children's Hospital Los Angeles, Los Angeles, CA, USA

³Pediatrics, Division of Neonatology, Children's Hospital Los Angeles, Los Angeles, CA, USA

⁴Harvard Medical School and Cardiovascular Research Center, Massachusetts General Hospital, Charlestown, MA, USA

⁵Martinos Center for Biomedical Imaging, Radiology, Massachusetts General Hospital, Charlestown, MA, USA

⁶ Biomedical Imaging Research Institute, Cedars-Sinai Medical Center, Los Angeles, CA, USA

Address Correspondence to:

Daeun Kim

University of Southern California

University Park Campus, 3710 McClintock Avenue, Ronald Tutor Hall (RTH) #317, Los Angeles, CA 90007.

Tel: (+1)213-300-1123

Email: daeunk@usc.edu

MANUSCRIPT BODY APPROXIMATE WORD COUNT = 5000

ABSTRACT

Purpose: Relaxation-Relaxation Correlation Spectroscopic Imaging (RR-CSI) is proposed to substantially improve the quality of multicomponent relaxation imaging.

Theory and Methods: Multicomponent relaxation imaging is a standard approach for identifying microstructural tissue components. However, due to ill-posedness, conventional approaches based on one dimensional relaxation encoding are unable to separate tissue compartments that have similar relaxation characteristics. Motivated by estimation theory and the “blessings of dimensionality,” RR-CSI instead acquires high-dimensional spatial-spectral data that nonseparably encodes information about multiple relaxation parameters for every spatial location. A high-dimensional spectroscopic image is then estimated by combining this high-dimensional data with an advanced spatial-spectral image reconstruction method, and spatial maps of different microstructural components are generated by integrating the spectral peaks.

Results: Simulations and experiments were performed to evaluate the features of RR-CSI, including the first-ever applications of this kind of approach to *in vivo* human brains. Results confirm that RR-CSI provides substantially more information than traditional lower-dimensional methods. The human results also demonstrate that RR-CSI is feasible for *in vivo* applications, and that RR-CSI identifies substantially more microstructural brain compartments than traditional approaches.

Conclusion: RR-CSI is a novel high-dimensional imaging approach that enables enhanced microstructure mapping capabilities.

KEYWORDS

Multicomponent Relaxometry; Microstructure Imaging; Multidimensional Correlation Spectroscopic Imaging; Constrained Reconstruction

INTRODUCTION

MRI is a powerful and versatile imaging modality, but ever since it was first introduced, its capabilities have always been practically limited by undesirable trade-offs between spatial resolution, signal-to-noise ratio (SNR), and data acquisition time. Due to these limitations, modern human MRI experiments are typically performed with millimeter-scale voxels, even though many scientifically- or clinically-interesting biological tissue features would only become directly visible at finer (e.g., microscopic or cellular) resolution scales.

Fortunately, the MRI community is ingenious and resourceful in the face of adversity, and spatial resolution barriers have not completely prevented the MRI-based study of tissue microstructure. Specifically, the past several decades have witnessed the development of many “indirect” MRI methods that allow us to probe microstructural tissue features without requiring microscopic-scale voxels. Generally speaking, these methods rely on the fact that certain MR contrast mechanisms, e.g., those based on diffusion characteristics (1–3) or relaxation characteristics (4–8), are sensitive to features of the local tissue microenvironment.

Among various MR microstructure imaging approaches, this paper focuses on a popular class of methods that perform multicomponent modeling of the MR relaxation signal (4, 6, 9–18). Such methods generally acquire several measurements from the same imaging voxel with different contrast settings, and then model the observed relaxation-based signal variations as a partial volume mixture of the distinct compartmental relaxation signatures (i.e., exponential decays) that would be observed from each of the sub-voxel microscopic tissue environments that comprise the voxel.

Most modern multicomponent relaxation imaging methods are based on one-dimensional (1D) relaxation contrast encoding (11–13, 19), in which a single sequence parameter such as the inversion time (TI) or echo time (TE) is varied to interrogate either T_1 , T_2 , or T_2^* relaxation characteristics. Many of these methods associate each voxel with a 1D relaxation “spectrum,” i.e., a continuous distribution of the different relaxation decay parameters that coexist within the voxel, where the different spectral peaks represent distinct relaxation decay characteristics and are often ascribed to distinct microstructural tissue compartments. Forming a “spectroscopic image” (comprising a distinct relaxation spectrum for every spatial

location) and plotting spatial maps of the integrated spectral peaks (11–13) can therefore provide important insights into the spatial distributions of different microstructural tissue compartments.

These one-dimensional (1D) spectroscopic imaging approaches can be very effective for some microstructure imaging applications. For example, myelin water imaging (11, 13) is a well-known approach that uses spectroscopic imaging based on T_2 relaxation to generate spatial maps describing the fractional myelin water content of each voxel. However, these 1D approaches also suffer from the ill-posedness of multi-exponential signal estimation (20), which has been recognized for centuries as a fundamentally difficult inverse problem (21). Practically, this ill-posedness means that it is extremely difficult to separate tissue compartments that have similar relaxation characteristics. For example, while the previously mentioned myelin water imaging approach (11, 13) is able to successfully isolate the signal associated with myelin water, it is unable to reliably distinguish between non-myelin white matter compartments and gray matter compartments because the T_2 values of these compartments are not distinct enough.

To address this fundamental problem, this paper proposes to use a higher-dimensional spectroscopic imaging approach, thereby leveraging some of the “blessings of dimensionality” (22) (e.g., that high-dimensional data can carry significantly more information content than low-dimensional data, and that high-dimensional data often possesses useful and exploitable structure that is not as common to observe in lower-dimensional settings). Specifically, we describe and investigate an approach that we call Relaxation-Relaxation Correlation Spectroscopic Imaging (RR-CSI), which leverages high dimensionality in several distinct and complementary ways. From a data acquisition perspective, RR-CSI acquires higher-dimensional data than conventional 1D approaches, including spatial dimensions as well as at least two relaxation encoding dimensions. From a signal modeling perspective, RR-CSI attempts to generate a higher-dimensional spectroscopic image, in which a distinct multidimensional relaxation correlation spectrum is associated with each voxel. And from an estimation perspective, RR-CSI uses a high-dimensional spatial-spectral estimation approach that leverages the spatial correlations that are expected to exist between neighboring spatial locations in the image, instead of estimating the relaxation spectrum independently for each

voxel. All of these components can be shown to reduce the ill-posedness of the inverse problem.

RR-CSI is built off of a significant amount of previous work. RR-CSI is partially motivated by our previous development of diffusion-relaxation correlation spectroscopic imaging (DR-CSI) (23), which is similar to RR-CSI except that it uses different contrast encoding mechanisms and different spectral dimensions. In particular, our previous implementation of DR-CSI (23) involved the combination of one relaxation dimension with one diffusion dimension, instead of using multiple relaxation dimensions as in RR-CSI. A key component of DR-CSI was the introduction of high-dimensional spatial-spectral estimation, which substantially reduced data sampling and quality requirements relative to the conventional voxel-by-voxel spectrum estimation methods that were widely used by previous diffusion-relaxation correlation spectroscopy (DR-COSY) methods (24–26). This innovation enabled DR-CSI to achieve the first ever spatial maps of microstructural tissue compartments derived from multidimensional correlation spectroscopy of exponential decay parameters. We make use of this same spatial-spectral estimation approach in RR-CSI.

RR-CSI is also partially inspired by previous relaxation-based correlation spectroscopy approaches (15, 16, 26–32), which we name relaxation-relaxation correlation spectroscopy (RR-COSY) following the terminology of Ref. (26). Just like RR-CSI, the RR-COSY approach uses data acquired with two-dimensional (2D) relaxation contrast encoding to estimate a 2D relaxation correlation spectrum that describes the joint distribution of T_1 and T_2 relaxation parameters within a sample (15, 16, 26–32). These previous contributions have already demonstrated that it is easier to separate microstructural compartments from 2D relaxation data than it is to separate them from 1D relaxation data.

Despite this important improvement in spectral resolving power, previous RR-COSY methods also suffer from some of the “curses of dimensionality” (22). For example, it is often substantially more time consuming to acquire 2D data than it is to acquire 1D data, since conventional sampling theory suggests that the number of measured data samples (and therefore data acquisition time) should grow exponentially with the dimension of the spectrum to be reconstructed. In addition, while RR-COSY is better-posed than 1D relaxometry, it is still an ill-posed problem, and data quality requirements are generally very high. In

part because of these data sampling and quality requirements, the vast majority of previous RR-COSY methods have never been used to generate high-quality spatial maps of the different microstructural tissue compartments that are visible within the 2D T_1 - T_2 correlation spectrum. One exception to this rule is the REDCO approach (33), which combined RR-COSY and DR-COSY ideas to generate an even higher-dimensional correlation spectrum, and leveraged a special constrained spectrum estimation approach (32) to reduce the required amount of data sampling. Nevertheless, despite the speed improvements gained from constrained spectrum estimation, the experimental protocol reported in Ref. (33) still required more than an hour to acquire the data needed to generate spatial maps for a single image slice, which would be a limiting factor for potential human applications. To the best of our knowledge, no previously reported RR-COSY methods have ever been fast enough to enable the practical *in vivo* spatial mapping of microstructural compartments in human subjects.

Our new RR-CSI method combines the multidimensional relaxation spectroscopy aspects of RR-COSY with the multidimensional spatial-spectral modeling and estimation approaches from DR-CSI. This combination enables RR-CSI to generate high-quality high-dimensional correlation spectroscopic images from a relatively small number of data samples. Importantly, the relative speed and robustness of our approach allows us to present the first ever spatial maps of *in vivo* microstructural tissue compartments derived from multidimensional relaxation spectroscopy of human subjects. Preliminary accounts of RR-CSI were previously presented in (34–36).

THEORY

For the sake of simplicity and without loss of generality, our description of RR-CSI will focus on the case that we have implemented for this paper, in which we estimate 2D T_1 - T_2 correlation spectra at every voxel, and assume that data is measured using an inversion-recovery spin-echo pulse sequence. Higher-dimensional implementations, implementations that use different contrast mechanisms, and implementations that use different pulse sequences are also possible as detailed (using substantially more complicated and less intuitive notation)

in our preliminary work (34).

Multidimensional Relaxation Spectroscopy and a Blessing of Dimensionality

In conventional relaxation spectroscopy methods, the measured signal from a macroscopic voxel is often modeled as a continuous distribution of different exponential decay parameters with no exchange between compartments. For example, in 1D T_2 -relaxometry based on a spin-echo acquisition (9,10), the ideal noiseless signal model can be represented as

$$m(TE) = \int f(T_2) e^{-TE/T_2} dT_2, \quad [1]$$

where $m(TE)$ is the ideal observed signal as a function of echo time (TE), and $f(T_2)$ is the continuous 1D spectrum of T_2 relaxation parameters that needs to be estimated from the data. Similarly, in T_1 -relaxometry based on an inversion recovery sequence (9,12), the ideal noiseless signal model can be represented as

$$m(TI) = \int f(T_1) (1 - 2e^{-TI/T_1}) dT_1, \quad [2]$$

where $m(TI)$ is the ideal observed signal as a function of inversion time (TI), and $f(T_1)$ is the continuous 1D spectrum of T_1 relaxation parameters that needs to be estimated from the data. In both cases, the 1D spectrum represents the fact that a macroscopic imaging voxel may be comprised of a large (potentially infinite!) number of microenvironments with distinct relaxation characteristics. And in both cases, data is acquired by varying a 1D contrast-encoding parameter, e.g., either TE or TI.

RR-COSY methods are based on the synergistic higher-dimensional combination of these lower dimensional models. For 2D T_1 - T_2 RR-COSY using an inversion-recovery spin-echo pulse sequence (29), the signal model becomes

$$m(TE, TI) = \int \int f(T_1, T_2) (1 - 2e^{-TI/T_1}) e^{-TE/T_2} dT_1 dT_2, \quad [3]$$

where it now becomes necessary to acquire 2D contrast-encoded data $m(TE, TI)$ in order to estimate the 2D T_1 - T_2 correlation spectrum $f(T_1, T_2)$. An important advantage of the 2D spectrum relative to the 1D spectrum is its capability to separate multiple compartments, even if some of the compartments have similar relaxation decay rates.

For illustration, consider the toy scenario depicted in Fig. 1 in which a voxel consists of three distinct compartments, where compartment 1 has $T_2 = 70$ ms and $T_1 = 750$ ms, compartment 2 has $T_2 = 100$ ms and $T_1 = 700$ ms, and compartment 3 has $T_2 = 110$ ms and $T_1 = 1000$ ms. These three spectral peaks are well-separated in the 2D T_1 - T_2 space, and therefore may be relatively straightforward to resolve. On the other hand, they are not well-separated when only considering the 1D T_2 dimension (i.e., compartments 2 and 3 may be hard to resolve because they have similar T_2 values) or only considering the 1D T_1 dimension (i.e., compartments 1 and 2 may be hard to resolve because they have similar T_1 values).

While the argument presented above is intuitive, previous literature has also empirically confirmed the advantages of RR-COSY over 1D relaxometry (15, 16, 26–32). Below, we present what we believe to be the first theoretical characterization of 2D RR-COSY relative to conventional 1D relaxation spectroscopy. Our theoretical characterization is based on the Cramér-Rao Lower bound (CRLB), which is a theoretical lower bound on the variance of an unbiased estimator for an unknown parameter of interest (37), and is frequently used to compare and optimize different experiment protocols in MR relaxometry (38–41). Since the CRLB depends on the specific values of the model parameters, our theoretical analysis is designed for the case of estimating the same toy three-compartment model described above, where the ideal noiseless data is given by

$$m(TE, TI) = \sum_{s=1}^3 f_s (1 - 2e^{-TI/T_1^s}) e^{-TE/T_2^s}, \quad [4]$$

where the spin density parameters f_s were all set equal to 1, and the T_1^s and T_2^s parameters were set to the T_1 and T_2 parameters given above for the three compartment model. Assuming white Gaussian noise, the CRLB is obtained by first computing the Fisher information matrix with respect to the unknown parameters that need to be estimated, and then

computing the matrix inverse of the Fisher information matrix (37–41).

When computing the CRLB for RR-COSY, we assumed that there were 9 unknown parameters to be estimated (i.e., the f_s , T_1^s , and T_2^s parameters for each compartment), while we assumed that there were 6 unknown parameters to be estimated for each 1D relaxometry experiment (e.g., only the f_s and T_1^s need to be estimated for each compartment in the T_1 -relaxometry case). The RR-COSY acquisition was assumed to use an inversion-recovery preparation for T_1 contrast encoding and a Carr-Purcell-Meiboom-Gill (CPMG) multi-spin echo sequence for T_2 contrast encoding, with data sampled at every combination of 7 inversion times ($TI = 0, 100, 200, 400, 700, 1000$ and 2000) and 15 echo times (TEs ranging from 7.5 ms to 217.5 ms in 15 ms increments) for a total of $7 \times 15 = 105$ contrast encodings. We compared against a conventional inversion recovery spin-echo sequence for T_1 relaxometry, using the same 7 inversion times used for RR-COSY. In this case, the expected scan time would be the same as for RR-COSY when the both sequences use the same TR. We also compared against conventional T_2 relaxometry using a standard CPMG-based multi-spin echo sequence with 32 echo times (TEs ranging from 10 ms to 320 ms). We assumed that this data was averaged 7 times, so that the experiment duration will match the duration of RR-COSY and T_1 relaxometry. For all three experiments, the noise standard deviation was assumed to be the same.

Comparing RR-COSY against 1D T_2 relaxometry, the CRLB calculation indicates that the lower bound on the standard deviation (i.e., the square root of the CRLB) achieved for T_2 with RR-COSY was 1.36×10^2 times smaller for the first compartment, 4.33×10^3 times smaller for the second compartment, and 9.50×10^3 times smaller for the third compartment. Comparing RR-COSY against 1D T_1 relaxometry, the CRLB calculation indicates that the lower bound on the standard deviation achieved for T_1 with RR-COSY was 1.07×10^5 times smaller for the first compartment, 2.67×10^4 times smaller for the second compartment, and 2.58×10^3 times smaller for the third compartment. As can be seen, the CRLB values for RR-COSY are orders-of-magnitude lower than either of the conventional 1D methods. These values lend strong estimation-theoretic support to the idea that 2D contrast encoding dramatically reduces the difficulty of estimating this kind of compartmental model relative to 1D encoding.

Spatial-Spectral Modeling and Another Blessing of Dimensionality

The previous subsection described and demonstrated the theoretical benefits of 2D relaxation encoding as in RR-COSY, but did not address the additional benefits that can be obtained by spatial-spectral modeling as in RR-CSI. Without loss of generality, we describe RR-CSI for the case where we perform 2D spatial encoding with spatial coordinates (x, y) . The spatial-spectral signal model for this case then becomes

$$m(x, y, TE, TI) = \int \int f(x, y, T_1, T_2)(1 - 2e^{-TI/T_1})e^{-TE/T_2} dT_1 dT_2, \quad [5]$$

where $m(x, y, TE, TI)$ represents the four-dimensional (4D) measured data, and $f(x, y, T_1, T_2)$ is the 4D spectroscopic image to be reconstructed.

The ability to potentially estimate a 4D spectroscopic image has multiple benefits. First, because the spectroscopic information is spatially resolved, it becomes possible to generate spatial maps describing the spatial distributions of the different peaks that are present in the spectrum. And second, if the spectral peak locations (but not necessarily the spin density associated with each spectral peak) are assumed to be similar for neighboring voxels, then using the data from multiple voxels to estimate the location of the shared spectral peak can have a similar effect to data averaging (42). In particular, analysis of a related problem has shown that joint spatial-spectral modeling (i.e., with the spectra for all voxels estimated simultaneously) has the potential to reduce the CRLB by an order of magnitude or more relative to uncoupled voxel-by-voxel estimation (42). This theoretical justification for spatial-spectral modeling has also been justified empirically in PET parameter estimation (42), 1D relaxometry (43, 44), and 2D DR-CSI (23).

This further reduction in the ill-posedness of the problem is important, because while RR-COSY is less ill-posed than 1D relaxometry, it is still an ill-posed problem. Generally speaking, RR-COSY methods require high-SNR and a large number of contrast encoded data samples in order to reconstruct a high-quality spectrum. In contrast, the use of spatial constraints allows these SNR and data sampling requirements to be relaxed, which enables high quality results from much shorter experiments (with fewer averages and fewer contrast encodings).

METHODS

High-Dimensional Spectroscopic Image Estimation

Based on the theory presented above, there are clear advantages to estimating a 4D spectroscopic image from 4D data using an estimation procedure that incorporates spatial constraints. We describe such an approach in this section. While the RR-CSI model in Eq. [5] is continuous, we will use a dictionary-based discrete model for practical numerical implementation. Note that dictionary-based approaches are standard in conventional 1D and 2D relaxation spectroscopy (9,13,29), and that our numerical implementation is also very similar to that we used with DR-CSI (23).

To enable the dictionary-based estimation, the integrals in Eq. [5] are replaced by standard Riemann sum approximations of the form:

$$m(x_i, y_i, TI_p, TE_p) = \sum_{q=1}^Q w_q f(x_i, y_i, T_1^q, T_2^q) (1 - 2e^{-TI_p/T_1^q}) e^{-TE_p/T_2^q}, \quad [6]$$

for $i = 1, \dots, N$ and $p = 1, \dots, P$. In this expression, N is the number of voxels in the image; (TI_p, TE_p) represents the contrast encoding parameters used in the p th acquisition, and it is assumed that we acquire P different contrast encodings; we have modeled the relaxation distribution using a dictionary with Q elements, where the q th element corresponds to the relaxation parameters (T_1^q, T_2^q) ; and w_q is the density normalization term (i.e., the numerical quadrature weights) required for accurate approximation of the continuous integral using a finite discrete sum. This discrete model can be equivalently represented in matrix form as

$$\mathbf{m}_i = \mathbf{K}\mathbf{f}_i, \quad [7]$$

for $i = 1, \dots, N$, where the vector $\mathbf{m}_i \in \mathbb{R}^P$ contains all the measured contrast-encoded data corresponding to the i th voxel and has p th entry $[\mathbf{m}_i]_p = m(x_i, y_i, TI_p, TE_p)$; the matrix $\mathbf{K} \in \mathbb{R}^{P \times Q}$ is a dictionary matrix that has entries $[K]_{pq} = w_q (1 - 2e^{-TI_p/T_1^q}) e^{-TE_p/T_2^q}$; and $\mathbf{f}_i \in \mathbb{R}^Q$ is the 2D spectrum corresponding to the i th voxel of the 4D spectroscopic image and has q th entry $[\mathbf{f}_i]_q = f(x_i, y_i, T_1^q, T_2^q)$.

Note that, to avoid the complexities that would be associated with phase modeling, we have assumed that we are working with real-valued magnitude images instead of complex-valued images, and that the different spectral peaks that coexist within the same voxel all share the same phase characteristics. These assumptions are standard in previous RR-COSY methods (15, 16, 26–32). One complication of using magnitude images is that the sampled values of the inversion recovery curve can be either positive or negative, but magnitude images will always be positive. However, the physics of T_1 relaxation tell us that the signed inversion recovery curve will always be monotonically increasing as a function of TI, while the magnitude images will appear to be decreasing when the true signal is negative and then start increasing after the zero-crossing point where the true signal is positive. In our implementation, we estimate this zero-crossing point and use this to apply polarity-correction to \mathbf{m}_i . In particular, we determine the zero-crossing point by polarity-correcting the signal curve using all possible negative-to-positive transition candidates, and then using the candidate that allows the polarity-corrected curve to have the smallest residual when the TI dimension is modeled as a monoexponential recovery curve.

In principle, it may be possible to solve for each spectrum \mathbf{f}_i in Eq. [7] by inverting the matrix \mathbf{K} . However, the columns of \mathbf{K} consist of highly-correlated exponential decays, and this matrix is very poorly conditioned. To partially mitigate the ill-posedness, the standard relaxation spectroscopy approach (used in both 1D relaxometry and in 2D RR-COSY) has been to impose a nonnegativity constraint on all elements of the relaxation spectrum together with additional Tikhonov regularization (10, 29) by solving

$$\hat{\mathbf{f}}_i = \arg \min_{\mathbf{f}_i \in \mathbb{R}^Q} \|\mathbf{m}_i - \mathbf{K}\mathbf{f}_i\|_2^2 + \|\mathbf{R}\mathbf{f}_i\|_2^2 \quad [8]$$

subject to $[\mathbf{f}]_q \geq 0$ for $\forall q = 1, \dots, Q$, where \mathbf{R} is an regularization matrix. For RR-CSI, we use the same nonnegativity constraint from classical relaxation spectroscopy methods while also using a spatial smoothness constraint similar to DR-CSI (23):

$$\left\{ \hat{\mathbf{f}}_1, \hat{\mathbf{f}}_2, \dots, \hat{\mathbf{f}}_N \right\} = \arg \min_{\{\mathbf{f}_i \in \mathbb{R}^Q\}_{i=1}^N} \left[\sum_{i=1}^N t_i \|\mathbf{m}_i - \mathbf{K}\mathbf{f}_i\|_2^2 + \lambda \sum_{l \in \Delta_i} \|\mathbf{f}_i - \mathbf{f}_l\|_2^2 \right] \quad [9]$$

subject to $[\mathbf{f}_i]_q \geq 0$ for $\forall q = 1, \dots, Q$ and $\forall i = 1, \dots, N$. The first term in this expression is a standard data consistency term for each voxel, similar to the first term of Eq. [8]. The second term is a spatial regularization term that encourages the 2D correlation spectrum from one voxel to be similar to the 2D correlation spectra from neighboring voxels, where Δi is the index set for the voxels that are directly adjacent to the i th voxel. The parameter λ is a user-selected regularization parameter that controls the strength of the spatial regularization. In the data consistency term, the variables t_i correspond to a spatial mask for the object, and are equal to 0 if the i th voxel is outside the object and are otherwise equal to one. This spatial mask is used to avoid fitting spectra to noise-only voxels of the image, and prevents spectra within the object from being contaminated by noise when spatial smoothness constraints are imposed. If we let $\mathbf{F} \in \mathbb{R}^{Q \times N}$ and $\mathbf{M} \in \mathbb{R}^{P \times N}$ represent the matrices whose i th columns respectively correspond to \mathbf{f}_i and \mathbf{m}_i , this optimization problem can also be more compactly be represented as

$$\hat{\mathbf{F}} = \arg \min_{\mathbf{F} \in \mathbb{R}^{Q \times N}} \|\mathbf{MT} - \mathbf{KFT}\|_F^2 + \lambda \|\mathbf{FC}^H\|_F^2, \quad [10]$$

subject to $[\mathbf{F}]_{pq} \geq 0$ for $\forall p = 1, \dots, P$ and $\forall q = 1, \dots, Q$. In this expression, $\|\cdot\|_F$ denotes the standard Frobenius norm, $\mathbf{T} \in \mathbb{R}^{N \times N}$ is a diagonal matrix whose i th diagonal entry contains the value of t_i , and \mathbf{C} is the matrix operator that computes spatial finite differences. It is worth noting that our spatially-constrained estimation technique can easily be adapted to other contrast mechanisms. For example, the DR-CSI reconstruction problem has the same form as Eq. [9], with the only difference being the form of the \mathbf{K} matrix (23).

Optimization Algorithm

The optimization problem in Eq. [9] is convex, and there are many convex optimization methods that will find the global solution from arbitrary initializations. In this work (and similar to our previous DR-CSI work (23)), we use an alternating directions method of multipliers (ADMM) algorithm to solve the nonnegativity-constrained optimization problem (45). We describe the steps of this algorithm below, but refer readers to Refs. (23, 45) for further detail.

- Set iteration number $j = 0$, and initialize $\hat{\mathbf{F}}^{(0)} \in \mathbb{R}^{Q \times N}$, $\hat{\mathbf{X}}^{(0)} \in \mathbb{R}^{Q \times N}$, $\hat{\mathbf{Y}}^{(0)} \in \mathbb{R}^{Q \times N}$,

$\hat{\mathbf{Z}}^{(0)} \in \mathbb{R}^{Q \times N}$, $\mathbf{G}^{(0)} \in \mathbb{R}^{Q \times N}$, $\mathbf{H}^{(0)} \in \mathbb{R}^{Q \times N}$ and $\mathbf{R}^{(0)} \in \mathbb{R}^{Q \times N}$ to arbitrary values. The variables \mathbf{X} , \mathbf{Y} , and \mathbf{Z} are used for variable splitting, while the variables \mathbf{G} , \mathbf{H} , and \mathbf{R} correspond to Lagrange multipliers. Also choose an augmented Lagrangian parameter value $\mu > 0$, which influences the convergence speed of ADMM but not the solution.

- At iteration $(j + 1)$:

1. For each $i = 1, \dots, N$, update the estimate of $\hat{\mathbf{f}}_i$ (i.e., the columns of $\hat{\mathbf{F}}$) according to

$$\hat{\mathbf{f}}_i^{(j+1)} = \begin{cases} \frac{1}{3} \left(\hat{\mathbf{x}}_i^{(j)} + \mathbf{g}_i^{(j)} + \hat{\mathbf{y}}_i^{(j)} + \mathbf{h}_i^{(j)} + \hat{\mathbf{z}}_i^{(j)} + \mathbf{r}_i^{(j)} \right), & \text{if } t_i = 1 \\ \frac{1}{2} \left(\hat{\mathbf{y}}_i^{(j)} + \mathbf{h}_i^{(j)} + \hat{\mathbf{z}}_i^{(j)} + \mathbf{r}_i^{(j)} \right), & \text{if } t_i = 0, \end{cases} \quad [11]$$

where $\hat{\mathbf{x}}_i^{(j)}$, $\mathbf{g}_i^{(j)}$, $\hat{\mathbf{y}}_i^{(j)}$, $\mathbf{h}_i^{(j)}$, $\hat{\mathbf{z}}_i^{(j)}$ and $\mathbf{r}_i^{(j)}$ are respectively the i th columns of $\hat{\mathbf{X}}^{(j)}$, $\mathbf{G}^{(j)}$, $\hat{\mathbf{Y}}^{(j)}$, $\mathbf{H}^{(j)}$, $\hat{\mathbf{Z}}^{(j)}$, and $\mathbf{R}^{(j)}$.

2. Set

$$\hat{\mathbf{X}}^{(j+1)} = (\mathbf{K}^H \mathbf{K} + \mu \mathbf{I})^{-1} \left(\mathbf{K}^H \mathbf{M} + \mu \left(\hat{\mathbf{F}}^{(j+1)} \mathbf{T} - \mathbf{G}^{(j)} \right) \right). \quad [12]$$

Note that the matrix $(\mathbf{K}^H \mathbf{K} + \mu \mathbf{I})$ is small and its inverse can easily be precomputed and stored for use in every iteration.

3. Set $\hat{\mathbf{Y}}^{(j+1)} = \hat{\mathbf{F}}^{(j+1)} - \mathbf{H}^{(j)}$, but replacing any negative values with zero.

4. Set

$$\hat{\mathbf{Z}}^{(j+1)} = \mu \left(\hat{\mathbf{F}}^{(j+1)} - \mathbf{R}^{(j)} \right) (\mu \mathbf{I} + \lambda \mathbf{C}^H \mathbf{C})^{-1}. \quad [13]$$

Note that if we assume periodic boundary conditions for the spatial smoothness regularization, then the matrices \mathbf{I} and $\mathbf{C}^H \mathbf{C}$ can both be diagonalized by the discrete Fourier transform, and we can use standard Fourier methods to quickly and analytically compute the desired matrix inversion result (45).

5. Set

$$\begin{aligned} \mathbf{G}^{(j+1)} &= \mathbf{G}^{(j)} - (\hat{\mathbf{F}}^{(j+1)} \mathbf{T} - \hat{\mathbf{X}}^{(j+1)}), \\ \mathbf{H}^{(j+1)} &= \mathbf{H}^{(j)} - (\hat{\mathbf{F}}^{(j+1)} - \hat{\mathbf{Y}}^{(j+1)}), \\ \text{and } \mathbf{R}^{(j+1)} &= \mathbf{R}^{(j)} - (\hat{\mathbf{F}}^{(j+1)} - \hat{\mathbf{Z}}^{(j+1)}). \end{aligned} \quad [14]$$

6. Set $j = j + 1$.
- Iterate steps 1-6 until convergence.

Evaluations

To evaluate RR-CSI, we have performed numerical simulations and real *in vivo* human brain experiments.

Numerical Simulations

For numerical simulation, a gold standard spectroscopic image was constructed using a three-compartment model according to

$$f(x, y, T_1, T_2) = \sum_{c=1}^3 a_c(x, y) f_c(T_1, T_2), \quad [15]$$

where $a_c(x, y)$ is the spatial distribution and $f_c(T_1, T_2)$ is the spectrum for the c th compartment, as shown in Fig. 2(a). The spectra were generated using a 2D Gaussian spectral lineshape with the same three spectral peak locations as in our previous theoretical CRLB example. Noiseless data was generated using the same set of 105 (TE, TI) combinations described previously. Subsequently, two datasets were generated with different levels of Gaussian noise, and magnitudes were taken leading to Rician-distributed data. Figures 2(b) and (c) respectively show representative images from the first (higher-SNR, with image SNRs ranging from 3.83 to 200) and second (lower-SNR, with image SNRs ranging from 1.05 to 80) datasets. The SNRs described above were computed separately for each contrast-encoded image as the ratio between the average signal intensity and the noise standard deviation.

For RR-CSI reconstruction, the a dictionary matrix \mathbf{K} was formed with every combination of 100 T_1 values (ranging from 100 ms to 3000 ms spaced logarithmically) and 100 T_2 values (ranging from 2 ms to 300 ms spaced logarithmically) for a total of $Q = 10,000$ dictionary elements. Optimization was performed using $\lambda = 0.01$, $\mu = 1$ and zero initialization. The optimization was performed using in-house MATLAB software.

To demonstrate the importance of spatial constraints, we also estimated 2D spectra voxel-

by-voxel using Eq. [8]. In addition, for comparison against 1D relaxometry, we simulated same the 1D T_1 relaxometry and 1D T_2 relaxometry acquisitions described in our previous theoretical CRLB example, with the noise level set consistent with the two RR-CSI datasets. As in the CRLB example, the T_2 relaxometry datasets were averaged seven times.

In vivo Human Brain Experiments

We acquired in vivo human brain RR-CSI data using an inversion recovery CPMG sequence on a 3T MRI scanner (Achieva; Philips Healthcare, Best, The Netherlands) with the following imaging parameters: 2 mm \times 2 mm in-plane resolution, $TR = 5000$ ms, a 32-channel receiver array coil, and SENSE parallel imaging with an acceleration factor of 2. Axial slices with 4 mm thickness and coronal slices with 2 mm thickness were acquired from four healthy subjects (3 females and 1 male, and age: 30 \sim 55 years). We acquired one axial and one coronal slice from subject 1, two axial slices and two coronal slices from subject 2, and two axial slices from both subjects 3 and 4. Contrast encoding used the same 105 (TE,TI) combinations described previously. Each single-slice dataset was acquired within 20 minutes. Spectroscopic image reconstruction was performed using the same RR-CSI parameters as in the previous simulations.

It should be noted that $TI = 0$ was not practical to implement, but it would theoretically produce the same sequence of magnitude images as a standard CPMG sequence without an inversion pulse. As a result, we acquired data corresponding to $TI = 0$ without using an inversion pulse and manually inverted the signal polarity. This procedure assumes perfect inversion of the longitudinal magnetization. However, the rest of RR-CSI data was acquired with a real inversion pulse, for which inversion efficiency may not be perfect due to various factors. In addition, the scanner also used a different (and unknown) scaling factor when saving images with an inversion pulse than it did when saving images without. As a result, the data corresponding to $TI = 0$ had different scaling compared to the rest of the data. To correct for this unknown scale factor, we fit a single-compartment (monoexponential) inversion recovery curve to the data acquired with $TI > 0$, and used this model to synthesize what the signal should have looked like at $TI = 0$. We compared this synthesized data against the measured data at $TI = 0$ to generate a scale factor for each voxel. A single global scale

correction was then obtained by averaging these voxelwise scale factors, and applied to the measured data at $TI = 0$.

To compare RR-CSI against a conventional 1D relaxometry method, we also used CPMG to acquire a dataset from one subject with 32 TEs ranging from 10 ms to 320 ms in 10 ms increments, and otherwise using the same imaging parameters described previously. This set of sequence parameters is typical for T_2 -based myelin water imaging (11, 13), and we chose to compare against this case because multicomponent T_2 relaxometry is more common in the literature than multicomponent T_1 relaxometry. Estimation of the 1D spectroscopic image was performed using the same basic RR-CSI optimization formulation from Eq. [10] (including spatial regularization), but modified so that we only had a 1D T_2 spectrum at each voxel (i.e., the spectroscopic image and the dictionary matrix were not functions of T_1).

RESULTS

Numerical Simulations

Figure 2 and Supporting Fig. S1 show the results from the numerical simulations. As can been seen in Figs. 2(d) and (f), two strong peaks and one weak peak are well-resolved in the spatially-averaged RR-CSI spectrum, and spatial maps obtained by integrating these three peaks in the spectral domain were well matched to the ground truth spatial maps. These observations were true at both noise levels.

In contrast, as can been seen in Figs. 2(e) and (g), we observe that voxel-by-voxel 2D spectrum estimation is less successful at recovering the original three peaks. In the high SNR case, an additional spectral peak observed between the peaks for components 1 and 2. In the low SNR case, the three different peaks are not very clearly separated. Spatial maps were derived from the voxel-by-voxel result using the same spectral integration regions that were used for RR-CSI. As can be seen, the spatial maps for each component also exhibit contamination from one or more of the other components, which is consistent with a failure to achieve sufficient spectral resolution.

Another important observation is that RR-CSI successfully resolved compartment 3 while

voxel-by-voxel estimation was substantially less successful. This occurred despite the fact that compartment 3 is not very spatially smooth, and spatial smoothness constraints are the only difference between RR-CSI and the voxel-by-voxel method. These results demonstrate the importance of using spatial constraints in RR-CSI to reduce the ill-posedness of the spectroscopic image estimation problem, and that the true spectroscopic image does not need to be very spatially smooth for these constraints to be useful.

Results from the 1D relaxometry simulations are shown in Supporting Fig. S1. As expected based on our previous analyses, both of the 1D relaxometry approaches failed to resolve three distinct spectral peaks, and were substantially less successful than the 2D approaches at recovering the spatial maps of the original three components.

In vivo Human Brain Experiments

For illustration, a representative single-slice 4D RR-CSI dataset comprising 105 different contrast encodings is shown in Fig. 3, with corresponding 2D RR-CSI spectra shown in Figure 4 and a visualization of the 4D RR-CSI spectroscopic image shown in Fig. 5.

As can be seen in Fig. 4, six spectral peaks were identified from the estimated 4D spectroscopic image. We believe that the capability to resolve six peaks is very encouraging, since conventional 1D relaxometry methods generally only resolve two or three different compartments. The ability of RR-CSI to resolve substantially more spectral peaks is consistent with our expectations about the superiority of high-dimensional encoding and estimation relative to lower-dimensional approaches.

As can be seen in Fig. 5, we also frequently observe multiple peaks coexisting within a single voxel, and the peaks each have their own distinct spatial distributions. If we ascribe the different spectral peaks to different microstructural tissue compartments, then we can interpret this 4D spectroscopic image as demonstrating the ability to resolve partial voluming and to spatially map the spatial variations of each compartment.

2D spectra obtained by spatially averaging the 4D RR-CSI spectroscopic image are shown for different slices and subjects in Figs. 6 (axial slices) and 7 (coronal slices). The number and spectral locations of the observed spectral peaks are largely the same as observed in the spectra shown in Fig. 4, demonstrating that the RR-CSI approach appears to yield robust

and consistent results across a range of different subjects and slice orientations.

Spatial maps obtained by spectrally integrating the six previously-identified spectral peaks are shown in Fig. 8 (axial slices), Supporting Fig. S2 (axial slices from a more superior portion of the brain), and Fig. 9 (coronal slices). We observe that these maps are also largely consistent with one another.

Importantly, the spatial maps also appear to qualitatively match well with known brain anatomy: component 1 seems to correspond to a white matter (WM) compartment; component 2 seems to correspond to GM structures with relatively high myelin content, including subcortical GM, putamen, thalamus and brainstem nuclei (as seen on the wall of the fourth ventricle in subject 1 in Fig. 9) as well as cortical GM; component 3 seems to correspond to brain structures with high iron content including the globus pallidus, subthalamic nucleus and substantia nigra; component 4 is similar to component 2, but seems to represent the GM content absent any myelin-content and notably does not include the subcortical GM; component 5 seems to correspond to cerebrospinal fluid (CSF); and component 6 resembles the myelin water compartment that has been observed in previous myelin water imaging experiments (11–13, 46).

It should be noted that the component 3 is not observed in every slice, which we believe is reasonable because the third compartment seems localized to gray matter structures like the globus pallidus, and these structures are not present in all of the slices we acquired data from.

It should also be noted that the relaxation parameter values we estimated for component 5 (which seems to correspond to CSF) and component 6 (which resembles myelin water) do not match the parameter values for these tissue types reported in previous literature (6, 8). This is somewhat expected, because the range of contrast encoding parameters we used may be insufficient to accurately estimate very quickly-relaxing tissues like myelin water or very slowly-relaxing tissues like CSF. Nevertheless, while the specific relaxation parameter values we've estimated are unlikely to be accurate, we are encouraged by the fact that it appears that RR-CSI may still be successfully resolving the spatial maps of these components.

For comparison against RR-CSI, Fig. 10 shows the results obtained from the 1D T_2 relaxometry experiment. As can be seen (and consistent with previous literature (11,13)),

only three spectral peaks are resolved, which is substantially fewer than the number of peaks resolved by RR-CSI. While the spatial maps corresponding to these three peaks all appear to be anatomically reasonable, we believe that the interpretation of these maps is less straightforward than the interpretation of the spatial maps from RR-CSI. In particular, we believe that the 1D relaxometry results are still substantially confounded by partial volume contributions, which appear to be more successfully resolved by RR-CSI.

DISCUSSION

This work described a novel high-dimensional approach to imaging microstructure and demonstrated, both theoretically and empirically, that this approach can have better compartmental resolving power than lower-dimensional approaches. However, using higher-dimensional contrast encoding is associated with practical increases in data acquisition time. While our human brain experiments were reasonably fast, a 20 minute acquisition may still be too long for routine practical use of this technique. However, there are still plenty of opportunities to make the scan faster. For example, while our acquisition used a relatively large number (i.e., 105) of different contrast encodings, it should be noted that this number of samples was not optimized, and was chosen based on the maximum number of contrasts we could fit within a 20 minute acquisition time. We have recently presented preliminary work that uses CRLB theory to optimize experimental protocols for both RR-CSI (47) and DR-CSI (48). This preliminary work has demonstrated that we can obtain similar-quality results with substantially less than 105 encodings, which may be leveraged to enable substantial improvements in data acquisition time. In addition, there have been other recent constrained reconstruction approaches that have been proposed to reduce the contrast-encoding requirements of high-dimensional relaxation spectroscopy (31–33), as well as constrained reconstruction approaches that have been proposed to reduce the k-space sampling and averaging requirements of multi-contrast imaging (49–52). Simultaneous-multislice imaging (53) could also be used to increase the volume coverage of an acquisition without increasing the acquisition time. All of these approaches could be combined with RR-CSI to further improve its speed.

It should also be noted that RR-CSI shares some similarities with some very recent multicomponent MR fingerprinting approaches (54, 55), which were developed concurrently and independently from RR-CSI. These fingerprinting methods also use multidimensional relaxation encoding, but use different signal modeling assumptions, different estimation techniques, and a very different style of data acquisition than RR-CSI. Comparing our human brain results with the human brain results presented in (54), it appears that our current RR-CSI implementation seems to resolve a substantially larger number of compartments in the brain tissues of normal subjects. Nevertheless, there are strong potentials for synergy between the RR-CSI and fingerprinting approaches, and a combination of these approaches may be a fruitful topic for future research.

Although our RR-CSI results appear to demonstrate successful decomposition of sub-voxel compartments from *in vivo* human subjects, some of the estimated relaxation parameters we estimated do not match closely with previous literature values. As explained previously, some of these discrepancies should be expected because our range of TEs and TIs may not be sufficient to accurately estimate very long or very short relaxation parameters. However, it is also known that quantification of relaxation parameters can be significantly affected by a variety of factors including experimental conditions, signal modeling, and optimization parameters, leading to mismatches even between different standard approaches (56). Recognizing these issues, we have focused on qualitative evaluation in real data scenarios rather than quantitative validation because of a lack of a gold standard. Nevertheless, we were able to show promising results in terms of reproducibility and consistency throughout the experiment of multiple subjects.

It is also worth noting that this work has focused on a proof-of-principle implementation to demonstrate the basic feasibility of RR-CSI. In this context, our RR-CSI implementation used a relatively simple acquisition and a relatively simple physics model. At this nascent stage, we intentionally avoided the consideration of complications such as water exchange, magnetization transfer, B1 inhomogeneity, B0 inhomogeneity, etc. Further exploration and development may lead to further improvements in RR-CSI reconstruction quality and/or enable the use of more advanced pulse sequences that may be more efficient than inversion-recovery CPMG but more sensitive to nonideal acquisition physics.

Lastly, it should be noted that our estimation formulation from Eq. [10] uses a least-squares penalty to enforce consistency. The use of least-squares is appropriate under a Gaussian noise model, although the magnitude images we used in this work are more properly modeled with a Rician distribution. While the differences between Gaussian noise and Rician noise are unlikely to matter very much in high-SNR regimes, it may be valuable to investigate the use of more accurate statistical noise modeling approaches like (57) in future work.

CONCLUSION

This work proposed and evaluated a novel microstructure imaging approach called RR-CSI. Our new approach combines high-dimensional contrast encoding with high-dimensional spatial-spectral image reconstruction to provide substantially improved imaging of microstructural tissue compartments from relatively coarse-resolution imaging data. Our results demonstrate the strong potential of RR-CSI using theoretical analysis, numerical simulations, and what we believe to be the first-ever *in vivo* human experiments of this kind.

ACKNOWLEDGMENTS

This work was supported in part by the USC Alfred E. Mann Institute and research grants NSF CCF-1350563, NIH R21 EB022951, NIH R01 NS074980, NIH R01 NS089212, and NIH R21 EB024701. Computation for some of the work described in this paper was supported by the University of Southern California's Center for High-Performance Computing (<http://hpcc.usc.edu/>). The authors thank Dr. Quin Lu from Philips Healthcare for clinical science support.

References

1. Jones DK, editor. *Diffusion MRI: Theory, Methods, and Applications*. Oxford: Oxford University Press. 2011.
2. Tournier JD, Mori S, Leemans A. Diffusion tensor imaging and beyond. *Magn Reson Med* 2011;65:1532–1556.
3. Le Bihan D, Johansen-Berg H. Diffusion MRI at 25 exploring brain tissue structure and function. *NeuroImage* 2012;61:324–341.
4. Fenrich F, Beaulieu C, Allen P. Relaxation times and microstructures. *NMR Biomed* 2001;14:133–139.
5. Koenig S, Brown R, Spiller M, Lundbom N. Relaxometry of brain: why white matter appears bright in MRI. *Magn Reson Med* 1990;14:482–495.
6. MacKay A, Laule C, Vavasour I, Bjarnason T, Kolind S, Mädler B. Insights into brain microstructure from the T2 distribution. *Magn Reson Imag* 2006;24:515–525.
7. Deoni SC. Quantitative relaxometry of the brain. *Top Magn Reson Imaging* 2010;21:101–113.
8. Does MD. Inferring brain tissue composition and microstructure via MR relaxometry. *NeuroImage* 2018;
9. Kroeker RM, Henkelman RM. Analysis of biological NMR relaxation data with continuous distributions of relaxation times. *J Magn Reson* 1986;69:218–235.
10. Whittall KP, MacKay AL. Quantitative interpretation of NMR relaxation data. *J Magn Reson* 1989;84:134–152.
11. MacKay A, Whittall K, Adler J, Li D, Paty D, Graeb D. In vivo visualization of myelin water in brain by magnetic resonance. *Magn Reson Med* 1994;31:673–677.
12. Labadie C, Lee JH, Vetek G, Springer CS. Relaxographic imaging. *J Magn Reson B* 1994;105:99–112.

13. Whittall KP, MacKay AL, Graeb DA, Nugent RA, Li DKB, Paty DW. In vivo measurement of T2 distributions and water contents in normal human brain. *Magn Reson Med* 1997;37:34–43.
14. Does MD, Beaulieu C, Allen PS, Snyder RE. Multi-component T1 relaxation and magnetisation transfer in peripheral nerve. *Magn Reson Med* 1998;16:1033–1041.
15. Saab G, Thompson RT, Marsh GD, Picot PA, Moran GR. Two-dimensional time correlation relaxometry of skeletal muscle in vivo at 3 tesla. *Magnetic resonance in medicine* 2001;46:1093–1098.
16. Does MD, Gore JC. Compartmental study of T1 and T2 in rat brain and trigeminal nerve in vivo. *Magn Reson Med* 2002;47:274–283.
17. Lancaster JL, Andrews T, Hardies LJ, Dodd S, Fox PT. Three-pool model of white matter. *J Magn Reson* 2003;17:1–10.
18. Deoni SC, Rutt BK, Arun T, Pierpaoli C, Jones DK. Gleaning multicomponent T1 and T2 information from steady-state imaging data. *Magn Reson Med* 2008;60:1372–1387.
19. Du YP, Chu R, Hwang D, Brown MS, Kleinschmidt-DeMasters BK, Singel D, Simon JH. Fast multislice mapping of the myelin water fraction using multicompartment analysis of T2* decay at 3T: a preliminary postmortem study. *Magn Reson Med* 2007;58:865–870.
20. Istratov AA, Vyvenko OF. Exponential analysis in physical phenomena. *Rev Sci Instrum* 1999;70:1233–1257.
21. Prony R. Essai experimental et analytique: sur les lois de la dilatabilite des fluides elastiques et sur celles de la force expansive de la vapeur de l'alkool, a differentes temperatures. *J L'Ecole Polytechnique* 1795;1:24–76.
22. Donoho DL. High-dimensional data analysis: The curses and blessings of dimensionality. In: *AMS Math Challenges Lecture*. 2000; .

23. Kim D, Doyle EK, Wisnowski JL, Kim JH, Haldar JP. Diffusion-relaxation correlation spectroscopic imaging: A multidimensional approach for probing microstructure. *Magn Reson Med* 2017;78:2236–2249.
24. Callaghan PT, Godefroy S, Ryland BN. Use of the second dimension in PGSE NMR studies of porous media. *Magn Reson Imag* 2003;21:243–248.
25. Hürlimann MD, Venkataraman L. Quantitative measurement of two-dimensional distribution functions of diffusion and relaxation in grossly inhomogeneous fields. *J Magn Reson* 2002;157:31–42.
26. Galvosas P, Callaghan PT. Multi-dimensional inverse Laplace spectroscopy in the NMR of porous media. *C R Physique* 2010;11:172–180.
27. Peemoeller H, Shenoy R, Pintar M. Two-dimensional NMR time evolution correlation spectroscopy in wet lysozyme. *J Magn Reson* 1981;45:193–204.
28. English A, Whittall K, Joy M, Henkelman R. Quantitative two-dimensional time correlation relaxometry. *Magn Reson Med* 1991;22:425–434.
29. Song Y, Venkataraman L, Hürlimann M, Flaum M, Frulla P, Straley C. T1-T2 correlation spectra obtained using a fast two-dimensional Laplace inversion. *J Magn Reson* 2002;154:261–268.
30. Celik H, Bouhrara M, Reiter D, Fishbein K, Spencer R. Stabilization of the inverse Laplace transform of multiexponential decay through introduction of a second dimension. *J Magn Reson* 2013;236:134–139.
31. Bai R, Cloninger A, Czaja W, Basser PJ. Efficient 2D MRI relaxometry using compressed sensing. *J Magn Reson* 2015;255:88–99.
32. Benjamini D, Basser PJ. Use of marginal distributions constrained optimization (MADCO) for accelerated 2D MRI relaxometry and diffusometry. *J Magn Reson* 2016; 271:40–45.

33. Benjamini D, Basser PJ. Magnetic resonance microdynamic imaging reveals distinct tissue microenvironments. *NeuroImage* 2017;163:183–196.
34. Kim D, Wisniewski JL, Haldar JP. MR correlation spectroscopic imaging of multidimensional exponential decays: probing microstructure with diffusion and relaxation. In: *Wavelets and Sparsity XVII, Proc. SPIE 10394*. 2017; p. 103940D.
35. Kim D, Wisniewski JL, Nguyen CT, Haldar JP. Multidimensional T1 relaxation-T2 relaxation correlation spectroscopic imaging (RR-CSI) for in vivo imaging of microstructure. In: *Proc. Int. Soc. Magn. Reson. Med.* 2018; p. 783.
36. Kim D, Wisniewski JL, Nguyen CT, Haldar JP. Probing in vivo microstructure with T1-T2 relaxation correlation spectroscopic imaging. In: *Proc. IEEE Int. Symp. Biomed. Imag.* 2018; pp. 675–678.
37. Kay SM. *Fundamentals of statistical signal processing*. Prentice Hall PTR. 1993.
38. Jones JA, Hodgkinson P, Barker AL, Hore PJ. Optimal sampling strategies for the measurement of spin-spin relaxation times. *J Magn Reson B* 1996;113:25–34.
39. Ogg RJ, Kingsley PB. Optimized precision of inversion-recovery T_1 measurements for constrained scan time. *Magn Reson Med* 2004;51:625–630.
40. Zhao B, Haldar JP, Liao C, Ma D, Griswold MA, Setsompop K, Wald LL. Optimal experiment design for magnetic resonance fingerprinting: Cramer-Rao bound meets spin dynamics. Preprint 2017;ArXiv:1710.08062.
41. Teixeira RPAG, Malik SJ, Hajnal JV. Joint system relaxometry (JSR) and Cramer-Rao lower bound optimization of sequence parameters: A framework for enhanced precision of DESPOT T_1 and T_2 estimation. *Magn Reson Med* 2018;79:234–245.
42. Lin Y, Haldar JP, Li Q, Conti PS, Leahy RM. Sparsity constrained mixture modeling for the estimation of kinetic parameters in dynamic PET. *IEEE Trans Med Imag* 2014; 33:173–185.

43. Kumar D, Nguyen TD, Gauthier SA, Raj A. Bayesian algorithm using spatial priors for multiexponential T2 relaxometry from multiecho spin echo MRI. *Magn Reson Med* 2012;68:1536–1543.
44. Labadie C, Lee JH, Rooney WD, Jarchow S, Aubert-Frécon M, Springer CS, Moller HE. Myelin water mapping by spatially regularized longitudinal relaxographic imaging at high magnetic fields. *Magn Reson Med* 2013;71:375–387.
45. Afonso MV, Bioucas-Dias JM, Figueiredo MA. An augmented Lagrangian approach to the constrained optimization formulation of imaging inverse problems. *IEEE Trans Image Process* 2011;20:681–695.
46. Oh SH, Bilello M, Schindler M, Markowitz CE, Detre JA, Lee J. Direct visualization of short transverse relaxation time component (ViSTA). *NeuroImage* 2013;83:485–492.
47. Kim D, Wisniewski JL, Haldar JP. Improved efficiency for microstructure imaging using high-dimensional MR correlation spectroscopic imaging. In: *Proc. Asilomar Conf. Sig. Sys. Comp.* 2017; pp. 1264–1268.
48. Kim D, Haldar JP. Faster diffusion-relaxation correlation spectroscopic imaging (DR-CSI) using optimized experiment design. In: *Proc. Int. Soc. Magn. Reson. Med.* 2017; p. 176.
49. Haldar JP, Liang ZP. Joint reconstruction of noisy high-resolution MR image sequences. In: *Proc. IEEE Int. Symp. Biomed. Imag.* 2008; pp. 752–755.
50. Gong E, Huang F, Ying K, Wu W, Wang S, Yuan C. PROMISE: Parallel-imaging and compressed-sensing reconstruction of multicontrast imaging using sharable information. *Magn Reson Med* 2015;73:523–535.
51. Zhao B, Lu W, Hitchens TK, Lam F, Ho C, Liang ZP. Accelerated MR parameter mapping with low-rank and sparsity constraints. *Magn Reson Med* 2015;74:489–498.
52. Bilgic B, Kim TH, Liao C, Manhard MK, Wald LL, Haldar JP, Setsompop K. Improving parallel imaging by jointly reconstructing multi-contrast data. *Magn Reson Med* 2018; 80:619–632.

53. Barth M, Breuer F, Koopmans PJ, Norris DG, Poser BA. Simultaneous multislice (SMS) imaging techniques. *Magn Reson Med* 2016;75:63–81.
54. McGivney D, Deshmane A, Jiang Y, Ma D, Badve C, Sloan A, Gulani V, Griswold M. Bayesian estimation of multicomponent relaxation parameters in magnetic resonance fingerprinting. *Magn Reson Med* 2018;80:159–170.
55. Tang S, Fernandez-Granda C, Lannuzel S, Bernstein B, Lattanzi R, Cloos M, Knoll F, Asslander J. Multicompartment magnetic resonance fingerprinting. preprint, arXiv:1802.10492.
56. Stikov N, Boudreau M, Levesque IR, Tardif CL, Barral JK, Pike GB. On the accuracy of T1 mapping: Searching for common ground. *Magn Reson Med* 2014;73:514–522.
57. Varadarajan D, Haldar JP. A majorize-minimize framework for Rician and non-central chi MR images. *IEEE Trans Med Imag* 2015;34:2191–2202.

Figure Captions

Figure 1: Toy illustration of the advantage of 2D RR-COSY over 1D relaxation spectroscopy. Ground truth values of three spectral peaks are shown in (a) a 2D T_1 - T_2 spectrum (left: a 3D plot and right: a 2D contour plot), (b) the corresponding 1D T_1 spectrum, and (c) the corresponding 1D T_2 spectrum. While the three peaks can all be successfully resolved in these example spectra, real experiments will experience degraded spectral resolution because of finite sampling and noise. When resolution is degraded, the three peaks can still be easily resolved in (d) the 2D spectrum, though are no longer well-resolved in (e,f) either of the 1D spectra.

Figure 2: (a) Ground truth used for numerical simulations: (left) compartmental spectra $f_c(T_1, T_2)$ and (right) compartment spatial maps $a_c(x, y)$. Representative (b) higher-SNR and (c) lower-SNR simulated images from the two different noise levels. In each dataset, the highest SNR image (corresponding to $TI = 0$ ms and $TE = 7.5$ ms) and the lowest SNR image (corresponding to $TI = 400$ ms and $TE = 217.5$ ms) are displayed. Estimation results are shown for (d) higher-SNR RR-CSI, (e) higher-SNR voxel-by-voxel 2D spectrum estimation, (f) lower-SNR RR-CSI, and (g) lower-SNR voxel-by-voxel 2D spectrum estimation. Each subfigure shows (left) the 2D spectrum obtained by spatially-averaging the 4D spectroscopic image and (right) spatial maps obtained by spectrally-integrating the spectral peak locations.

Figure 3: A representative single-slice 4D RR-CSI dataset (the axial slice from subject 1) comprising 105 different contrast encodings.

Figure 4: RR-CSI spectra estimated from the axial slice from subject 1. (left) The 2D spectrum obtained by spatially averaging the 4D RR-CSI spectroscopic image. (middle) Representative individual spectra plotted from different voxels. Component 1 and component 6 are plotted from a white matter voxel (red), component 2 is plotted from a voxel in the putamen (green), component 3 is plotted from a voxel in the globus pallidus (cyan), component 4 is plotted from a voxel in gray matter (blue), and component 5 is plotted from

a voxel in the cerebral spinal fluid (yellow). In this, each of the spectral peaks has been numbered and color-coded (red: component 1, green: component 2, cyan: component 3, blue: component 4, yellow: component 5, and magenta: component 6. This color coding scheme was also used to depict the individual voxel locations on (right) an anatomical reference image.

Figure 5: Visualization of the estimated 4D RR-CSI spectroscopic image from the axial slice of subject 1. Spatially-varying 2D RR-CSI spectra are shown from (left) the entire image (81×74 voxels), (middle) a subregion of the entire image corresponding to the green box (16×16 voxels), and (right) an even smaller subregion corresponding to the orange box (5×4 voxels). In each 2D spectrum, the horizontal axis corresponds to the T_2 dimension and the vertical axis corresponds to the T_1 dimension. Each spectrum is color-coded based on the six spectral peaks and the color-coding scheme described in Fig. 4.

Figure 6: Reference images (corresponding to $TI = 0$ and $TE = 7.5$ ms) and spatially-averaged RR-CSI spectra from different axial slices of different subjects.

Figure 7: Reference images (corresponding to $TI = 0$ and $TE = 7.5$ ms) and spatially-averaged RR-CSI spectra from different coronal slices of different subjects.

Figure 8: Spatial maps obtained by spectrally-integrating the six spectral RR-CSI peaks from axial slices of different subjects. Each map is color-coded based on the scheme from Fig. 4, and the composite image is also shown on the right.

Figure 9: Spatial maps obtained by spectrally-integrating the six spectral RR-CSI peaks from coronal slices of different subjects. Each map is color-coded based on the scheme from Fig. 4, and the composite image is also shown on the right.

Figure 10: Results from conventional 1D T_2 relaxation. (a) The 1D spectrum obtained by spatially-averaging the 3D spectroscopic image. (b) Representative 1D spectrum from a

voxel in white matter. (c) Spatial maps obtained by spectrally-integrating the three spectral peak locations. Each map is color-coded (magenta: comp.A, green: comp.B, and yellow: comp.C), and the composite image is also shown on the right.

Supporting Figure Captions

Figure S1: Estimation results corresponding to simulated 1D T_1 relaxometry and 1D T_2 relaxometry acquisitions. Estimation results are shown for (a) higher-SNR T_1 relaxometry, (b) higher-SNR T_2 relaxometry, (c) lower-SNR T_1 relaxometry, and (d) lower-SNR T_2 relaxometry. The different columns show (left) the 1D spectra obtained by spatially-averaging the 3D spectroscopic image, (middle) representative single-voxel spectra, and (right) spatial maps obtained by spectrally-integrating the spectral peak locations.

Figure S2: Spatial maps obtained by spectrally-integrating the six spectral RR-CSI peaks from superior axial slices of different subjects. Each map is color-coded based on the scheme from Fig. 4, and the composite image is also shown on the right.

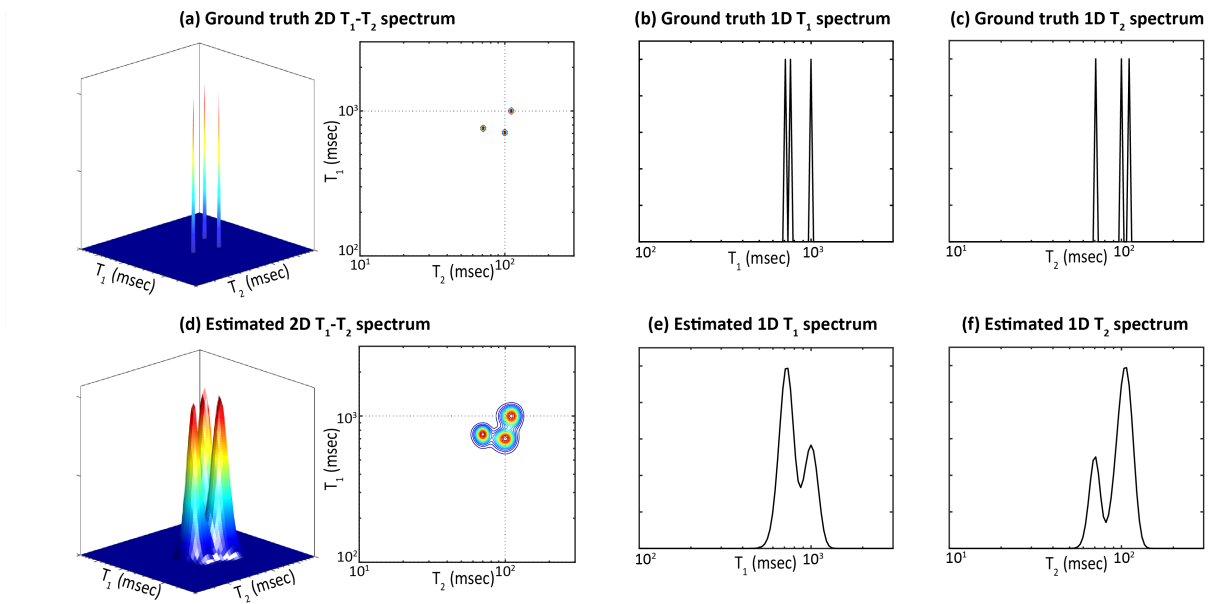


Figure 1: Toy illustration of the advantage of 2D RR-COSY over 1D relaxation spectroscopy. Ground truth values of three spectral peaks are shown in (a) a 2D T_1 - T_2 spectrum (left: a 3D plot and right: a 2D contour plot), (b) the corresponding 1D T_1 spectrum, and (c) the corresponding 1D T_2 spectrum. While the three peaks can all be successfully resolved in these example spectra, real experiments will experience degraded spectral resolution because of finite sampling and noise. When resolution is degraded, the three peaks can still be easily resolved in (d) the 2D spectrum, though are no longer well-resolved in (e,f) either of the 1D spectra.

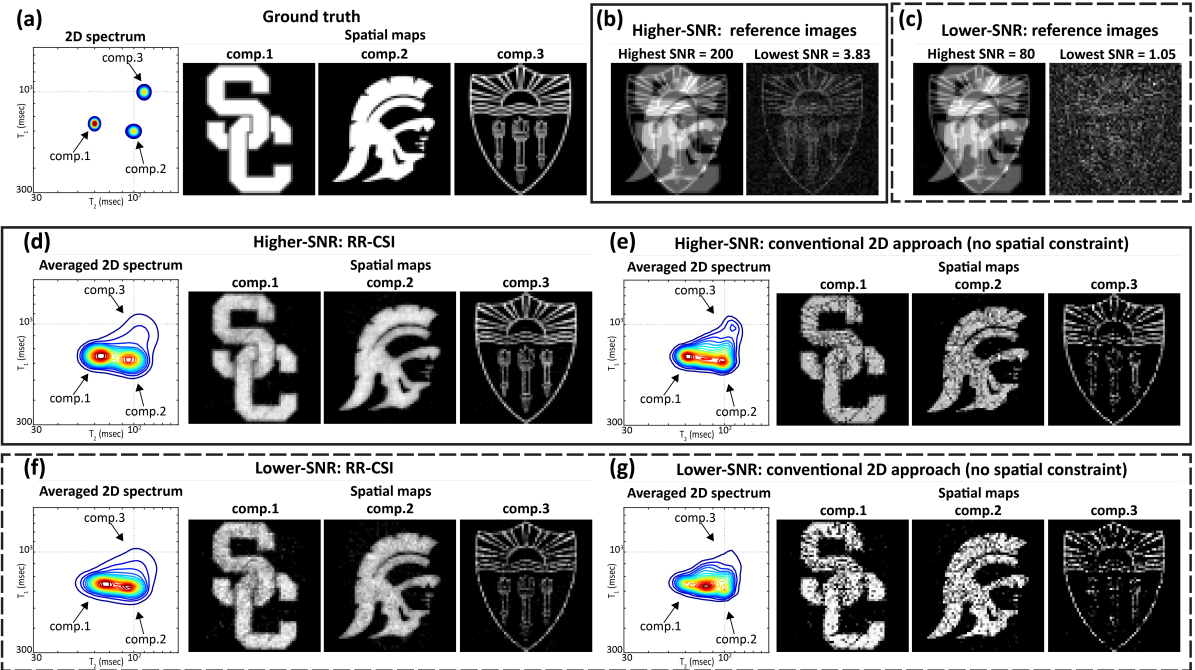


Figure 2: (a) Ground truth used for numerical simulations: (left) compartmental spectra $f_c(T_1, T_2)$ and (right) compartment spatial maps $a_c(x, y)$. Representative (b) higher-SNR and (c) lower-SNR simulated images from the two different noise levels. In each dataset, the highest SNR image (corresponding to $TI = 0$ ms and $TE = 7.5$ ms) and the lowest SNR image (corresponding to $TI = 400$ ms and $TE = 217.5$ ms) are displayed. Estimation results are shown for (d) higher-SNR RR-CSI, (e) higher-SNR voxel-by-voxel 2D spectrum estimation, (f) lower-SNR RR-CSI, and (g) lower-SNR voxel-by-voxel 2D spectrum estimation. Each subfigure shows (left) the 2D spectrum obtained by spatially-averaging the 4D spectroscopic image and (right) spatial maps obtained by spectrally-integrating the spectral peak locations.

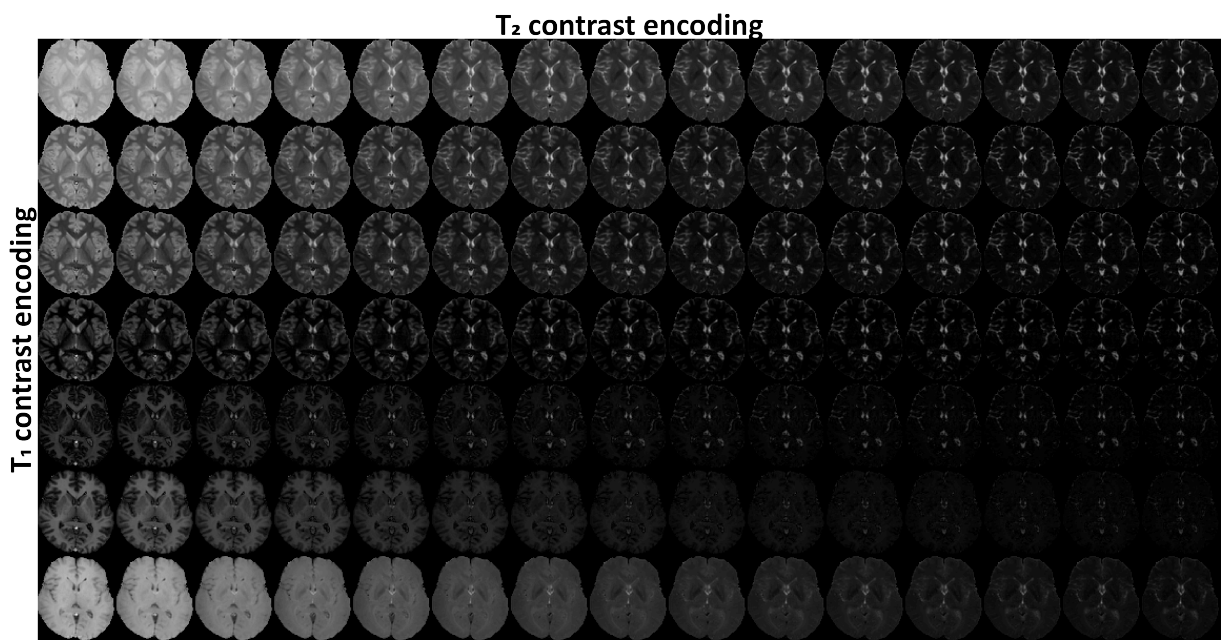


Figure 3: A representative single-slice 4D RR-CSI dataset (the axial slice from subject 1) comprising 105 different contrast encodings.

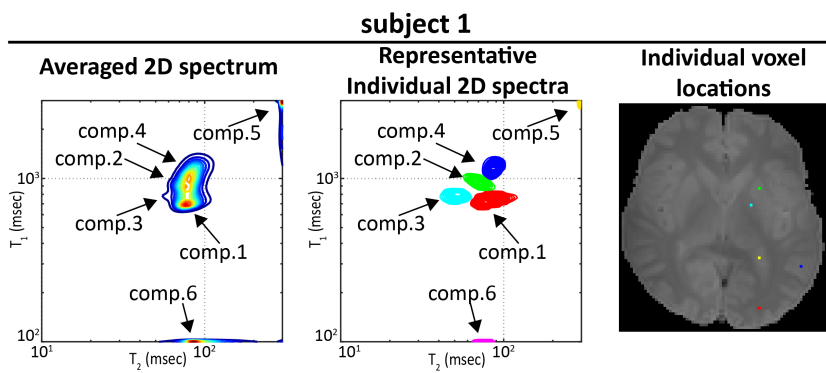


Figure 4: RR-CSI spectra estimated from the axial slice from subject 1. (left) The 2D spectrum obtained by spatially averaging the 4D RR-CSI spectroscopic image. (middle) Representative individual spectra plotted from different voxels. Component 1 and component 6 are plotted from a white matter voxel (red), component 2 is plotted from a voxel in the putamen (green), component 3 is plotted from a voxel in the globus pallidus (cyan), component 4 is plotted from a voxel in gray matter (blue), and component 5 is plotted from a voxel in the cerebral spinal fluid (yellow). In this, each of the spectral peaks has been numbered and color-coded (red: component 1, green: component 2, cyan: component 3, blue: component 4, yellow: component 5, and magenta: component 6). This color coding scheme was also used to depict the individual voxel locations on (right) an anatomical reference image.

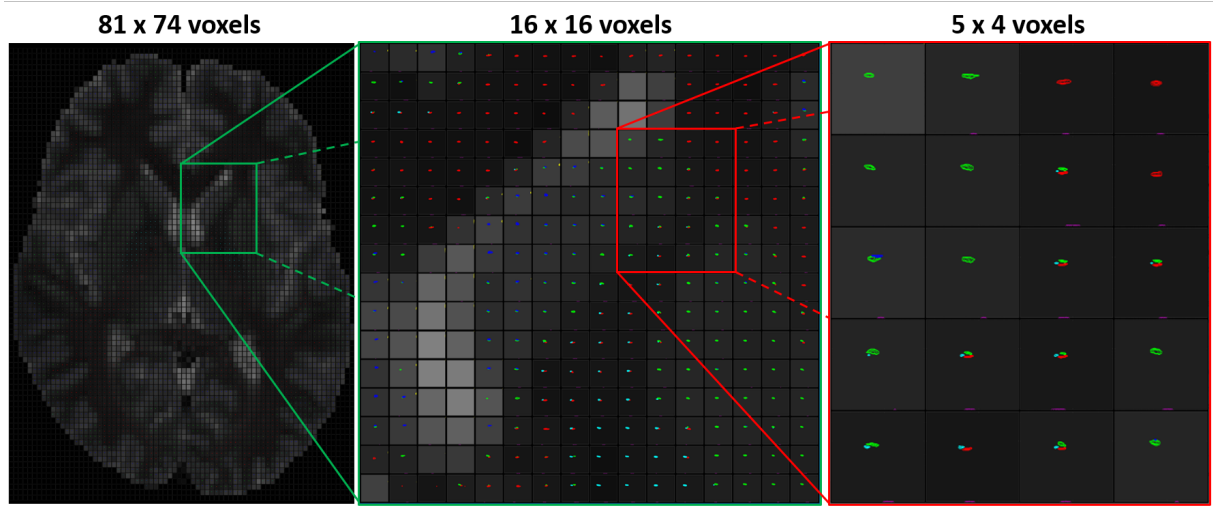


Figure 5: Visualization of the estimated 4D RR-CSI spectroscopic image from the axial slice of subject 1. Spatially-varying 2D RR-CSI spectra are shown from (left) the entire image (81×74 voxels), (middle) a subregion of the entire image corresponding to the green box (16×16 voxels), and (right) an even smaller subregion corresponding to the orange box (5×4 voxels). In each 2D spectrum, the horizontal axis corresponds to the T_2 dimension and the vertical axis corresponds to the T_1 dimension. Each spectrum is color-coded based on the six spectral peaks and the color-coding scheme described in Fig. 4.

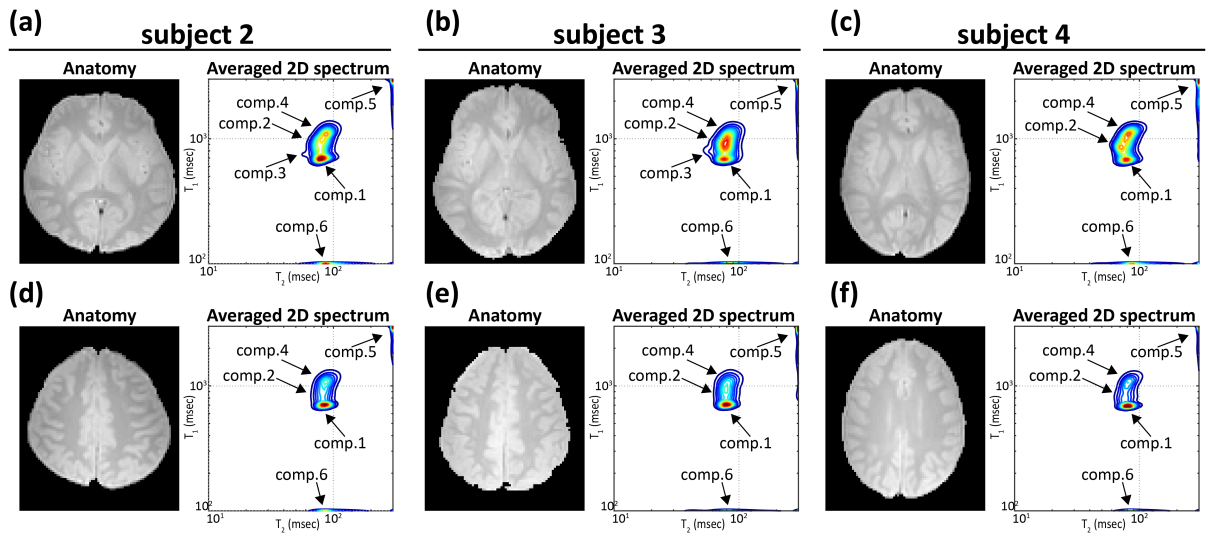


Figure 6: Reference images (corresponding to $TI = 0$ and $TE = 7.5$ ms) and spatially-averaged RR-CSI spectra from different axial slices of different subjects.

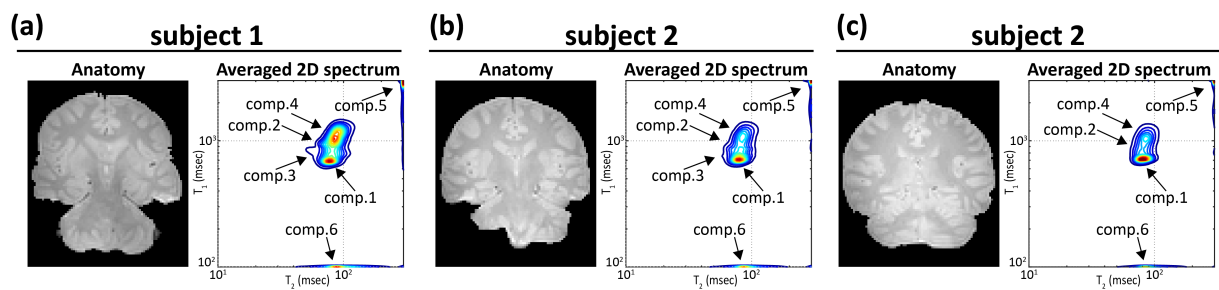


Figure 7: Reference images (corresponding to $TI = 0$ and $TE = 7.5$ ms) and spatially-averaged RR-CSI spectra from different coronal slices of different subjects.

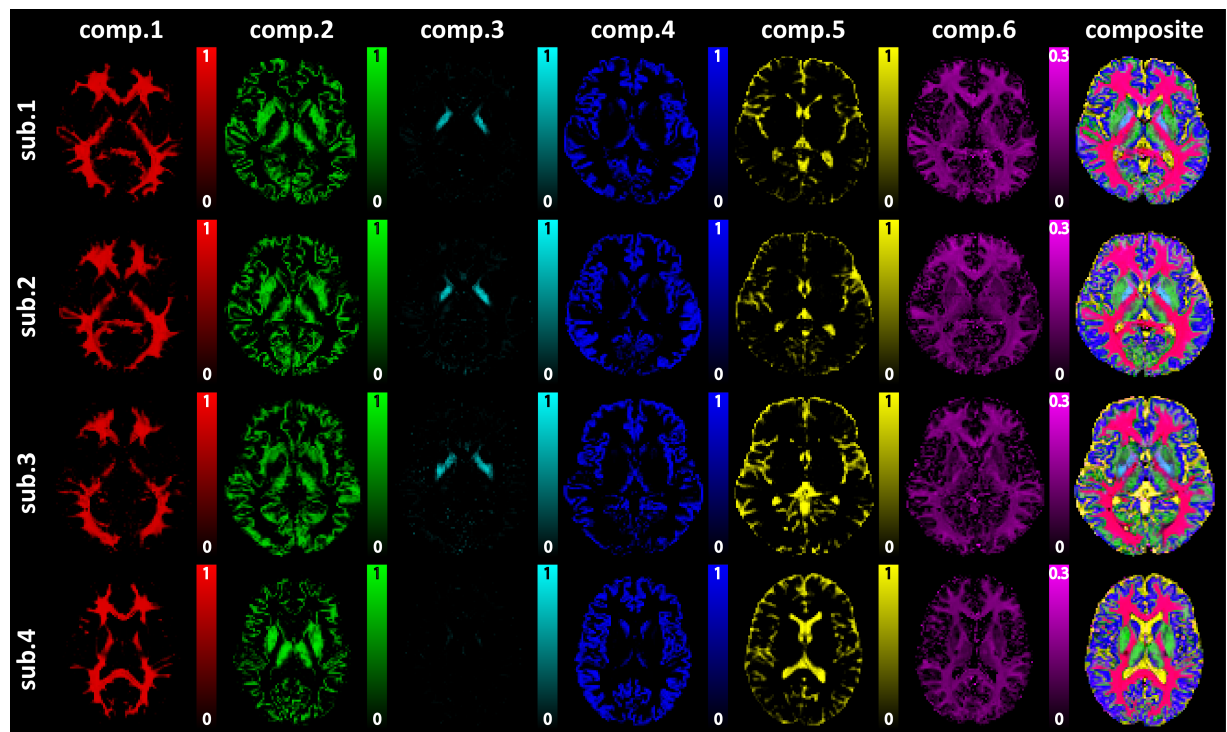


Figure 8: Spatial maps obtained by spectrally-integrating the six spectral RR-CSI peaks from axial slices of different subjects. Each map is color-coded based on the scheme from Fig. 4, and the composite image is also shown on the right.

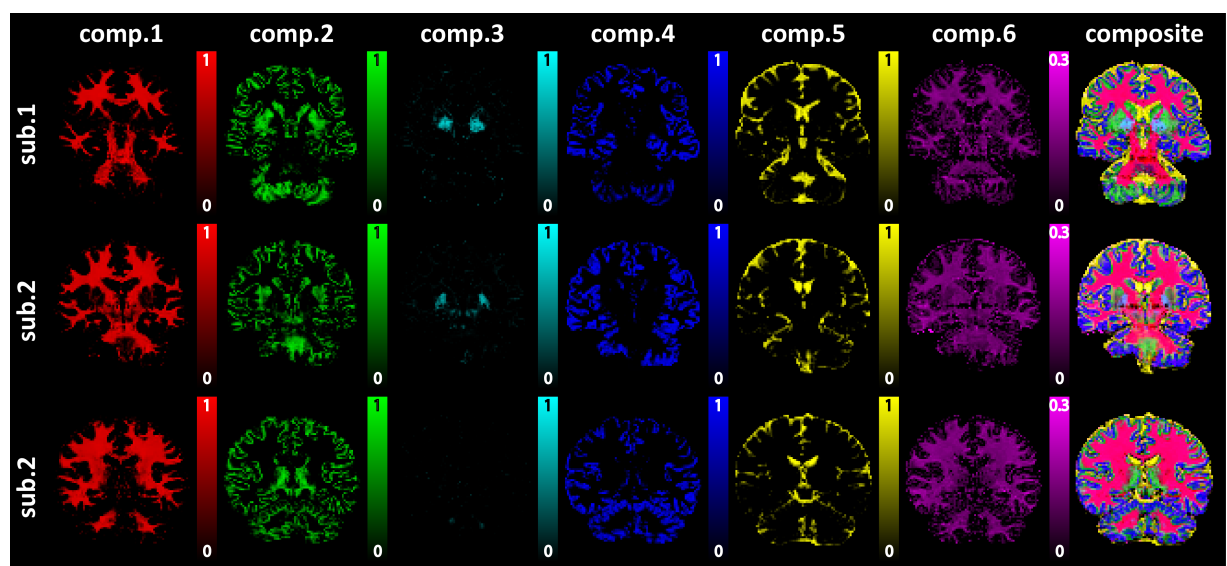


Figure 9: Spatial maps obtained by spectrally-integrating the six spectral RR-CSI peaks from coronal slices of different subjects. Each map is color-coded based on the scheme from Fig. 4, and the composite image is also shown on the right.

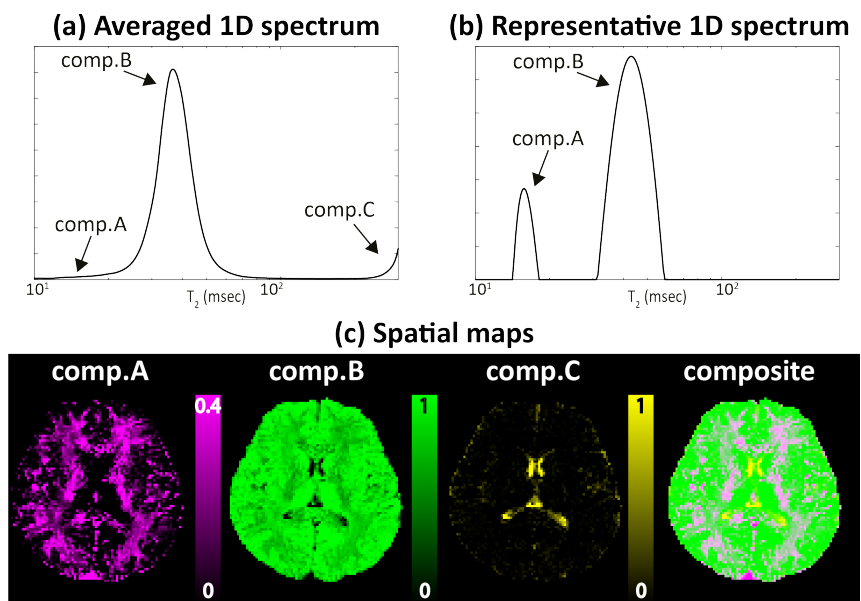


Figure 10: Results from conventional 1D T_2 relaxation. (a) The 1D spectrum obtained by spatially-averaging the 3D spectroscopic image. (b) Representative 1D spectrum from a voxel in white matter. (c) Spatial maps obtained by spectrally-integrating the three spectral peak locations. Each map is color-coded (magenta: comp.A, green: comp.B, and yellow: comp.C), and the composite image is also shown on the right.

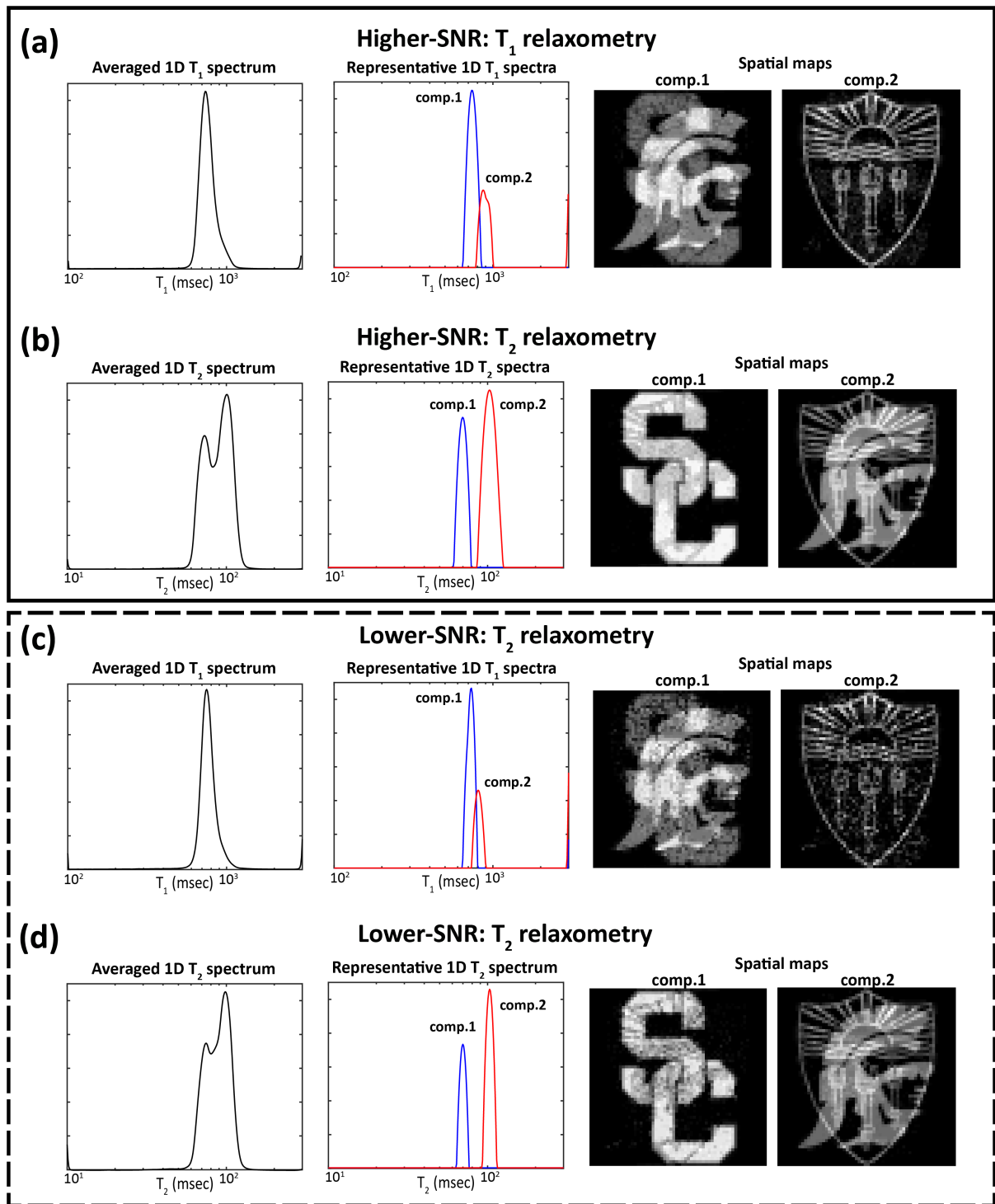


Figure S1: Estimation results corresponding to simulated 1D T_1 relaxometry and 1D T_2 relaxometry acquisitions. Estimation results are shown for (a) higher-SNR T_1 relaxometry, (b) higher-SNR T_2 relaxometry, (c) lower-SNR T_1 relaxometry, and (d) lower-SNR T_2 relaxometry. The different columns show (left) the 1D spectra obtained by spatially-averaging the 3D spectroscopic image, (middle) representative single-voxel spectra, and (right) spatial maps obtained by spectrally-integrating the spectral peak locations.

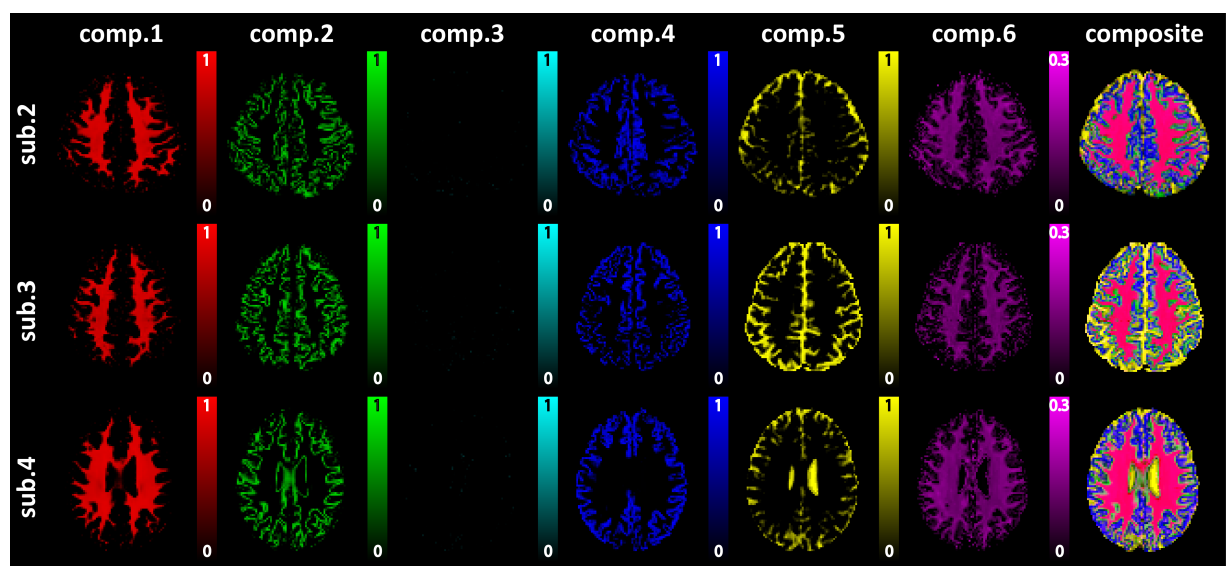


Figure S2: Spatial maps obtained by spectrally-integrating the six spectral RR-CSI peaks from superior axial slices of different subjects. Each map is color-coded based on the scheme from Fig. 4, and the composite image is also shown on the right.